

Day-side z'-band emission and eccentricity of WASP-12b¹

Mercedes López-Morales^{2,4}, Jeffrey L. Coughlin^{3,5}, David K. Sing⁶, Adam Burrows⁷, Dániel Apai⁸, Justin C. Rogers^{4,9}, David S. Spiegel⁷ & Elisabeth R. Adams¹⁰

e-mail: mercedes@dtm.ciw.edu

ABSTRACT

We report the detection of the eclipse of the very-hot Jupiter WASP-12b via z'-band time-series photometry obtained with the 3.5-meter ARC telescope at Apache Point Observatory. We measure a decrease in flux of $0.082 \pm 0.015\%$ during the passage of the planet behind the star. That planetary flux is equally well reproduced by atmospheric models with and without extra absorbers, and blackbody models with $f \geq 0.585 \pm 0.080$. It is therefore necessary to measure the planet at other wavelengths to further constrain its atmospheric properties. The eclipse appears centered at phase $\phi = 0.5100_{-0.0061}^{+0.0072}$, consistent with an orbital eccentricity of $|e \cos \omega| = 0.016_{-0.009}^{+0.011}$ (see note at end of §4). If the orbit of the planet is indeed eccentric, the large radius of WASP-12b can be explained by tidal heating.

¹Based on observations collected with the Apache Point Observatory 3.5-meter telescope, which is owned and operated by the Astrophysical Research Consortium (ARC).

²Hubble Fellow

³NSF Graduate Research Fellow

⁴Carnegie Institution of Washington, Department of Terrestrial Magnetism, 5241 Broad Branch Rd. NW, Washington D.C., 20015, USA

⁵Department of Astronomy, New Mexico State University, Las Cruces, NM 88003, USA

⁶Astrophysics group, School of Physics, University of Exeter, Stocker Road, Exeter, Ex4 4QL, United Kingdom

⁷Princeton University, Department of Astrophysical Sciences, Peyton Hall, Princeton, NJ, 08544, USA

⁸Space Telescope Science Institute, 3700 San Martin Drive, Baltimore, MD 21218, USA

⁹Johns Hopkins University, Department of Physics and Astronomy, 366 Bloomberg Center, 3400 N. Charles Street, Baltimore, MD 21218, USA

¹⁰Department of Earth, Atmospheric and Planetary Sciences, Massachusetts Institute of Technology, 77 Massachusetts Ave., Cambridge, MA, 02139

Subject headings: planetary systems — stars: individual: WASP-12— techniques: photometric

1. Introduction

The transiting Very Hot Jupiter WASP-12b, discovered by Hebb et al. (2009), has many notable characteristics. With a mass of $1.41 \pm 0.10 M_{Jup}$ and a radius of $1.79 \pm 0.09 R_{Jup}$, WASP-12b is the planet with the second largest radius reported to date. It is also the most heavily irradiated planet known, with an incident stellar flux at the substellar point of over $9 \times 10^9 \text{ erg cm}^{-2} \text{ s}^{-1}$. In addition, model fits to its observed radial velocity and transit light curves suggest that the orbit of WASP-12b is slightly eccentric. All these attributes make WASP-12b one of the best targets to test current irradiated atmosphere and tidal heating models for extrasolar planets.

In irradiated atmosphere model studies WASP-12b is an extreme case even in the category of highly irradiated gas giants. Such highly irradiated planets are expected to show thermal inversions in their upper atmospheric layers (Burrows et al. 2008), although the chemicals responsible for such inversions remain unknown. TiO and VO molecules, which can act as strong optical absorbers, have been proposed (Hubeny et al. 2003; Fortney et al. 2008), but Désert et al. (2008) claim that the concentration of those molecules in planetary atmospheres is too low ($< 10^{-3} - 10^{-2}$ times solar). Spiegel et al. (2009) argue that TiO needs to be at least half the solar abundance to cause thermal inversions, and very high levels of macroscopic mixing are required to keep enough TiO in the upper atmosphere of planets. S_2 , S_3 and HS compounds have also recently been suggested and then questioned as causes of the observed thermal inversions (Zahnle et al. 2009a,b).

In the case of tidal heating, detailed models are now being developed (e.g. Bodenheimer et al. 2003; Miller et al. 2009; Ibgui et al. 2009,b; Ibgui & Burrows 2009) to explain the inflated radius phenomenon observed in hot Jupiters, of which WASP-12b, with a radius over 40% larger than predicted by standard models, is also an extreme case. All models assume that the planetary orbits are slightly eccentric, and directly measuring those eccentricities is key not only to test the model hypotheses, but also to obtain information about the planets' core mass and energy dissipation mechanisms (see e.g. Ibgui et al. 2009).

Here we present the detection of the eclipse of WASP-12b in the z' -band ($0.9 \mu\text{m}$), which gives the first measurement of the atmospheric emission of this planet, and the first direct estimation of its orbital eccentricity. Section 2 summarizes the observations and analysis of

the data. In Section 3 we compare the emission of the planet to models. The results are discussed in Section 4.

2. Observations and Analyses

We monitored WASP-12 [RA(J2000)=06:30:32.794, Dec(J2000)=+29:40:20.29, V=11.7] during two eclipses, and under photometric conditions, on February 19 and October 18 2009 UT. An additional attempt on October 30 2009 UT was lost due to weather. The data were collected with the SPICam instrument on the ARC’s 3.5-meter telescope at Apache Point Observatory, using a SDSS z' filter with an effective central wavelength of $\sim 0.9\mu\text{m}$. SPICam is a backside-illuminated SiTe TK2048E 2048x2048 pixel CCD with 24 micron pixels, giving an unbinned plate scale of 0.14 arc seconds per pixel and a field of view of 4.78 arc minutes square. The detector, cosmetically excellent and linear through the full A/D converter range, was binned 2x2, which gives a gain of $3.35\text{ e}^-/\text{ADU}$, a read noise of 1.9 DN/pixel, and a 48 second read time.

On February 19 we monitored WASP-12 from 3:00 to 3:28 UT and from 3:54 to 7:10 UT, losing coverage between 3:28 and 3:54 UT when the star reached a local altitude greater than 85° , the soft limit of the telescope at that time. These observations yielded 1.20 hours of out-of-eclipse and 2.45 hours of in-eclipse coverage, at airmasses between 1.005–1.412. On October 18 we extended the altitude soft limit of the telescope to 87° and covered the entire eclipse from 7:05 to 12:45 UT, yielding 2.73 hours of out-of-eclipse and 2.93 hours of in-eclipse coverage, with airmasses between 1.001–1.801. In both nights we defocused the telescope to a FWHM of $\sim 2''$ to reduce pixel sensitivity variation effects, and also to allow for longer integration times, which minimized scintillation noise and optimized the duty cycle of the observations. Pointing changed by less than $(x,y)=(4,7)$ pixels in the October 18 dataset, and by less than $(x,y)=(3,12)$ pixels on February 19, with the images for this second night suffering a small gradual drift in the y direction throughout the night. Integration times ranged from 10 to 20 seconds. Taking into account Poisson, readout, and scintillation noise, the photometric precision on WASP-12 and other bright stars in the images ranged between 0.07–0.15% per exposure on February 19, and between 0.05–0.09% per exposure on October 18.

The field of view of SPICam was centered at RA(J2000)=06:30:25, Dec(J2000)=+29:42:05 and included WASP-12 and two other isolated stars at RA(J2000)=06:30:31.8, Dec(J2000)=+29:42:27 and RA(J2000)=06:30:22.6, Dec(J2000)=+29:44:42, with apparent brightness and $B-V$ and $J-K$ colors similar to the target. Each night’s dataset was analyzed independently and the results combined in the end. The timing information was extracted from the headers of the

images and converted into Heliocentric Julian Days using the IRAF task *setjd*, which has been tested to provide sub-second timing accuracy.

We corrected each image for bias-level and flatfield effects using standard IRAF routines. Dark current was negligible. DAOPHOT-type aperture photometry was performed in each frame. We recorded the flux from the target and the comparison stars over a wide range of apertures and sky background annuli around each star. We used apertures between 2 and 35 pixels in one-pixel steps during a first preliminary photometry pass, and 0.05 pixel steps in the final photometric extraction. To compute the sky background around each star we used variable width annuli, with inner radii between 35 and 60 pixels sampled in one-pixel steps.

The best aperture and sky annuli combinations were selected by identifying the most stable (i.e. minimum standard deviation), differential light curves between each comparison and the target at phases out-of-eclipse¹. In the February 19 data, the best photometry results from an aperture radius of 14.7 pixels for both the target and the comparison stars, and sky annuli with a 52-pixel inner radius and 22-pixel wide. For the October 18 data, 17.9 pixel apertures and sky annuli with a 45-pixel inner radius and 22-pixel wide produce the best photometry.

The resultant differential light curves between the target and each comparison contain systematic trends that can be attributed to either atmospheric effects, such as airmass, seeing, or sky brightness variations, or to instrumental effects, such as small changes in the location of the stars on the detector. Systematics can also be introduced by instrumental temperature or pressure changes, but those parameters are not monitored in SPICam. We modeled systematics for each light curve by fitting linear correlations between each parameter (airmass, seeing, sky brightness variations, and target position) and the out-of-eclipse portions of the light curves. All detected trends are linear and there are no apparent residual color difference effects. The full light curves are then de-trended using those correlation fits. In the October 18 dataset, airmass effects are the dominant systematic, introducing a linear baseline trend with an amplitude in flux of 0.07%. The February 19 dataset also shows systematics with seeing and time with a total amplitude of also 0.07%. The systematics on this night were modeled using only the after-eclipse portion of the light curve, and we consider this dataset less reliable than the October 18 one. The 18 pre-ingress images collected between 3:00 and 3:38 UT suffer from a ~ 50 pixel position shift with respect to the rest of the images collected that night, which cannot be modeled using overall out-of-eclipse

¹We had to iterate on the out-of-eclipse phase limits after finding that the eclipse was centered at $\phi = 0.51$. Out-of-eclipse was finally defined as phases $\phi < 0.45$ and $\phi > 0.57$.

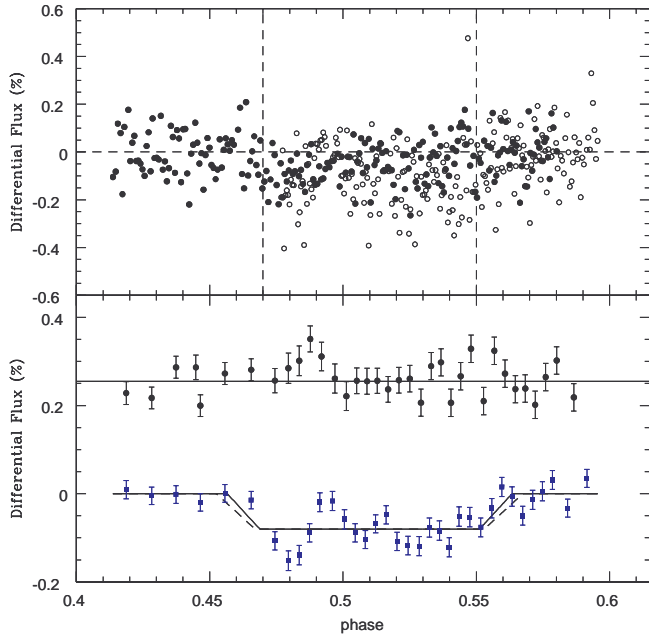


Fig. 1.— *Top*: De-trended differential light curves. Open and filled dots show, respectively, the Feb 19 and Oct 18 UT 2009 data. *Bottom*: Combined light curves binned by a factor of 12. Blue squares correspond to WASP-12 and black dots to the differential light curve of the two comparison stars. The best fit models are shown as solid lines (for $e = 0$) and dashed lines (for $e = 0.057$). Both models produce the same depth and center phase, but the $e = 0.057$ model lasts 11.52 minutes longer. We attribute the flux jumps between phases 0.475 and 0.5 to unremoved systematics. Notice that, although the systematics appear in both curves, the trends in each curve are not correlated in phase.

systematics. We chose not to use those points in the final analysis. Correlations with the other parameters listed above are not significant in any of the two datasets.

Finally, we produce one light curve per night by combining the de-trended light curves of each comparison. The light curves are combined applying a weighted average based on the Poisson noise of the individual light curve points. The result is illustrated in Figure 1. The out-of-eclipse scatter of the combined light curves is 0.11% for the February 19 data and 0.09% for the October 18 data. De-trending significantly improves the systematics, but some unidentified residual noise sources remain, which we have not been able to fully model.

2.1. Eclipse detection and error estimation

The two-night combined light curve contains 421 points between phases 0.413 and 0.596, based on the Hebb et al. (2009) ephemerides. To establish the presence of the eclipse and its parameters, we fit the data to a grid of models generated using the *JASMINE* code, which combines the Kipping (2008) and Mandel & Agol (2002) algorithms to produce model light curves in the general case of eccentric orbits. The models do not include limb darkening and use as input parameters the orbital period, stellar and planetary radii, argument of the periastron, orbital inclination, stellar radial velocity amplitude and semi-major axis values derived by Hebb et al. (2009). The eccentricity is initially assumed to be $e=0$, which produces models with a total eclipse duration of 2.808 hours. The best fit model is found by χ^2 minimization, with the depth, the central phase of the eclipse, and the out-of-eclipse differential flux as free parameters.

First we fit the individual night light curves to ensure the eclipse signal is present in each dataset. The February 19 data give an eclipse depth of $0.100 \pm 0.023\%$, while the derived eclipse depth for the October 18 data is $0.068 \pm 0.021\%$. The central phases are $\phi=0.510$ for the first eclipse and $\phi = 0.508$ for the second. We assume the difference in depth is due to systematics we have not been able to properly model. The incomplete eclipse from February 19 might seem more prone to systematics, but our inspection of both datasets does not reveal stronger trends in that dataset. We therefore combined the data from both nights, weighting each light curve based on its out-of-eclipse scatter.

The result of the combined light curve analysis is the detection of an eclipse with a depth of $0.082 \pm 0.015\%$ and centered at orbital phase $\phi = 0.51$, as shown in Figure 1. The reduced χ^2 of the fit is 0.952. The error in the eclipse depth is computed using the equation $\sigma_{depth}^2 = \sigma_w^2/N + \sigma_r^2$, where σ_w is the scatter per out-of-eclipse data point and σ_r^2 describes the red noise. The σ_r is estimated with the binning technique by Pont et al. (2006) to be 1.5×10^{-4} when binning on timescales up to the ingress and egress duration of about 20 minutes.

We investigate to what extent the uncertainties in the system’s parameters affect our eclipse depth and central phase results. Varying the impact parameter, planet-to-star ratio, and scale of the system by 1σ of the reported values in Hebb et al. (2009), the measured eclipse depth changes only by 0.004% or $0.27\sigma_{depth}$, while the central phase remains unchanged. Our result is therefore largely independent of the adopted system parameters.

We performed three other tests to confirm the eclipse detection in a manner similar to previously reported eclipse results (Deming et al. 2005; Sing & López-Morales 2009; Rogers et al. 2009). From the average of the 125 out-of-eclipse light curve data points versus

the 228 in-eclipse points (only points where the planet is fully eclipsed, adopting $\phi=0.51$ as the central eclipse phase), we measure an eclipse depth of $0.080 \pm 0.015\%$. We further check the detection by producing histograms of the normalized light curve flux distribution in the in-eclipse and out-of-eclipse portions of the light curve. The result, illustrated in Figure 2, shows how the flux distribution of in-eclipse points is shifted by 0.00082 with respect to the out-of-eclipse flux distribution, centered at zero. The results of the last test, where we use a new set eclipse of models with a duration corresponding to $e = 0.057$, fix the out-of-eclipse baseline to zero, and leave both depth and central phase of the eclipse as a free parameters, are shown in Figure 3. The two top panels in the figure show 1-D cuts of each parameter through the z (normalized χ^2), space, where $z=0$ gives the best fit model and $z=1$ defines the 1σ confidence interval of the result (see definition of z in §3 of López-Morales & Bonanos 2008; Behr 2003). However, inspection of the eclipse depth in Figure 1 reveals that the 1σ errors from this method ($\pm 0.036\%$) are too large. To estimate more realistic errors for the central phase, we generate contours plots (bottom panel in Fig. 3), where the 1σ eclipse depth error has been fixed to the 0.015% value derived above. The resultant center phase is $\phi = 0.5100_{-0.0061}^{+0.0072}$. We also applied prayer-bead, bootstrapping, and Markov-Chain Monte Carlo (MCMC) error analysis techniques (Gillon et al. 2007; Southworth 2008) to estimate the errors in the central phase of the eclipse. The MCMC analysis contained 2.85×10^6 links, and we adopted the 1.5×10^{-4} photometric error (~ 1.6 times the formal error), given by the Pont et al. (2006) binning technique. All these give central phases within $\phi = 0.5100_{-0.0036}^{+0.0030}$. The larger error in the central phase given by the normalized χ^2 method suggests the presence of correlated noise in the data, which the other methods might not be correctly accounting for. We therefore adopt these larger errorbars in our final estimation of the central phase.

2.2. Eccentricity

The eccentricity e of WASP-12b was calculated from the measured central phase shift value using eq. (6) from Wallenquist (1950),

$$e \cos \omega = \frac{\pi (t_2 - t_1 - P/2)}{P (1 + \csc^2 i)}, \quad (1)$$

where P , i and ω are, respectively, the orbital period, inclination, and periastron angle of the system, and $t_2 - t_1$ is the time difference between transit and eclipse. In our case $t_2 - t_1 = 0.51P$. Using the values of P , i and ω from Hebb et al. (2009), we derive an $e = 0.057_{-0.034}^{+0.040}$, which agrees with the non-zero eccentricity result reported by these authors. This eccentricity can be in principle explained if 1) the system is too young to have already circularized, 2) there are additional bodies in the system pumping the eccentricity of WASP-12b, or 3) the tidal dissipation factor Q'_P (Goldreich 1963) of WASP-12b is several orders of

magnitude larger than Jupiter’s, estimated to be between 6×10^4 and 2×10^6 (Yoder & Peale 1981).

3. Comparison with atmospheric models

We compare the observed z' -band flux of WASP-12b to simple blackbody models and to expectedly more realistic radiative-convective models of irradiated planetary atmospheres in chemical equilibrium, following the same procedure described in Rogers et al. (2009). The results are shown in Figures 4 and 5.

In the simplistic blackbody approximation, a $0.082 \pm 0.015\%$ deep eclipse corresponds to a z' -band brightness temperature of $T_{z'} \sim 3028_{-110}^{+99} K$, slightly lower than the planet’s equilibrium temperature of $T_p \sim 3129 K$ assuming zero Bond albedo ($A_B = 0$) and no energy reradiation ($f = 2/3$) (see López-Morales & Seager 2007). However, when the thermal and reflected flux of the planet are included, different combinations of A_B and f can yield the same eclipse depth, as illustrated in Figure 4. From that figure we can constrain the energy redistribution factor to $f \geq 0.585 \pm 0.080$, but the albedo is not well constrained. Assuming a maximum $A_B \leq 0.4$, the temperature of the day-side of WASP-12b is $T_p > 2707 K$.

The more realistic atmospheric models are derived from self-consistent coupled radiative transfer and chemical equilibrium calculations, based on the models described in Sudarsky et al. (2000, 2003), Hubeny et al. (2003) and Burrows et al. (2005, 2006, 2008) (see Rogers et al. 2009, for details). We generate models with and without thermal inversion layers, by adding an unidentfied optical absorber between 0.43 and 1.0 μm , with different level of opacity κ' . The opacity of the absorber varies parabolically with frequency, with a peak value of $\kappa' = 0.25 \text{ cm}^2 \text{ gr}^{-1}$. As Figure 5 shows, models with and without extra absorbers produce similar fits to the observed z' -band flux. The best model without absorber has a $P_n = 0.3^2$. The best model with an extra absorber has a $P_n = 0.1$ and $\kappa_e = 0.1 \text{ cm}^2 \text{ gr}^{-1}$. Observations at other wavelengths are necessary to further constrain the models.

² $P_n = 0$ and $P_n = 0.5$ correspond, respectively, to $f = 2/3$ and $f = 1/4$, however there is not well defined $P_n - f$ relation for intermediate values since the physical models account for atmospheric parameters (e.g. pressure, opacity) in a way different than blackbody models.

4. Discussion and Conclusions

This first detection of the eclipse of WASP-12b agrees with the slight eccentricity of the planet’s orbit found by Hebb et al. (2009), and places initial constraints to its atmospheric characteristics.

The presence of other bodies in the system can be tested via radial velocity or transit timing variation observations, although the current RV curve by Hebb et al. (2009) shows no evidence of additional planets, unless they are in very long orbits.

One would expect that if extra absorbers are present in the upper atmosphere of the planet in gaseous form, they might give rise to thermal inversion layers. However, as Figure 5 illustrates, the observed $0.9 \mu\text{m}$ eclipse depth can be fit equally well by a model without extra absorbers. Additional observations at longer wavelengths, specially longer than $\sim 4.0 \mu\text{m}$, will break that model degeneracy. Observations at wavelengths below $\sim 0.6 \mu\text{m}$ will also place better constraints on A_B .

Note: While this paper was in the final revision stages, two new secondary eclipse observations from *Spitzer* were reported by Campo et al. (2010). They find secondary eclipse central phases consistent with a circular orbit. We have carefully reviewed our analysis and still arrive to a slightly eccentric orbit, although the result is only significant at the $1.4\text{--}1.6\sigma$ confidence level. Possible explanations proposed by Campo et al. (2010) for the measured eccentricity difference are orbital precession or wavelength-dependent brightness variations across the surface of the planet that would shift the center of the eclipse. A similar effect has been recently suggested by Swain et al. (2010) on the surface of HD189733b. Further observations are needed to establish whether this discrepancy is a data artifact or a real effect.

M.L.M. acknowledges support from NASA through Hubble Fellowship grant HF-01210.01-A/HF-51233.01 awarded by the STScI, which is operated by the AURA, Inc. for NASA, under contract NAS5-26555. J.L.C acknowledges support from a NSF Graduate Research Fellowship. A.B. is supported in part by NASA grant NNX07AG80G. D.A. and J.C.R. are grateful for support from STScI Director’s Discretionary Research Fund D0101.90131. This work has been supported by NSF’s grant AST-0908278.

REFERENCES

Behr, B. B. 2003, *ApJS*, 149, 67

- Barnes, R. et al. 2009, ArXiv e-prints
- Bodenheimer, P. et al. 2003, ApJ, 592, 555
- Burrows, A., Budaj, J., & Hubeny, I. 2008, ApJ, 678, 1436
- Burrows, A., Hubeny, I., & Sudarsky, D. 2005, ApJ, 625, L135
- Burrows, A., Sudarsky, D., & Hubeny, I. 2006, ApJ, 650, 1140
- Campo, C. J., Harrington, J., Hardy, R. A., Stevenson, K. B., Nymeyer, S., Ragozzine, D., Lust, N. B., Anderson, D. R., Collier-Cameron, A., Blečić, J., Britt, C. B. T., Bowman, W. C., Wheatley, P. J., Deming, D., Hebb, L., Hellier, C., Maxted, P. F. L., Pollaco, D., & West, R. G. 2010, ArXiv e-prints
- Deming, D. et al. 2005, Nature, 434, 740
- Désert, J. et al. 2008, A&A, 492, 585
- Fortney, J. J. et al. 2008, ApJ, 678, 1419
- Gillon, M. et al. 2007, A&A, 471, L51
- Goldreich, R. 1963, MNRAS, 126, 257
- Hebb, L. et al. 2009, ApJ, 693, 1920
- Hubeny, I., Burrows, A., & Sudarsky, D. 2003, ApJ, 594, 1011
- Ibgui, L. & Burrows, A. 2009, ApJ, 700, 1921
- Ibgui, L., Burrows, A., & Spiegel, D. S. 2009, ArXiv e-prints
- Ibgui, L., Spiegel, D. S., & Burrows, A. 2009b, ArXiv e-prints
- Kipping, D. M. 2008, MNRAS, 389, 1383
- López-Morales, M. & Seager, S. 2007, ApJ, 667, L191
- López-Morales, M. & Bonanos, A. Z. 2008, ApJ, 685, L47
- Mandel, K. & Agol, E. 2002, ApJ, 580, L171
- Miller, N., Fortney, J. J., & Jackson, B. 2009, ApJ, 702, 1413
- Pont, F., Zucker, S., & Queloz, D. 2006, MNRAS, 373, 231

- Rogers, J. C. et al., 2009, ArXiv e-prints
- Sing, D. K. & López-Morales, M. 2009, A&A, 493, L31
- Southworth, J. 2008, MNRAS, 386, 1644
- Spiegel, D. S., Silverio, K., & Burrows, A. 2009, ApJ, 699, 1487
- Sudarsky, D., Burrows, A., & Hubeny, I. 2003, ApJ, 588, 1121
- Sudarsky, D., Burrows, A., & Pinto, P. 2000, ApJ, 538, 885
- Swain, M. R. et al., 2010, Nature, 463, 637
- Wallenquist, Å. 1950, Arkiv for Astronomi, 1, 59
- Yoder, C. F. & Peale, S. J. 1981, Icarus, 47, 1
- Zahnle, K. et al. 2009a, AAS Meeting Abstracts, Vol. 214, 306.01
- Zahnle, K. et al. 2009b, ApJ, 701, L20

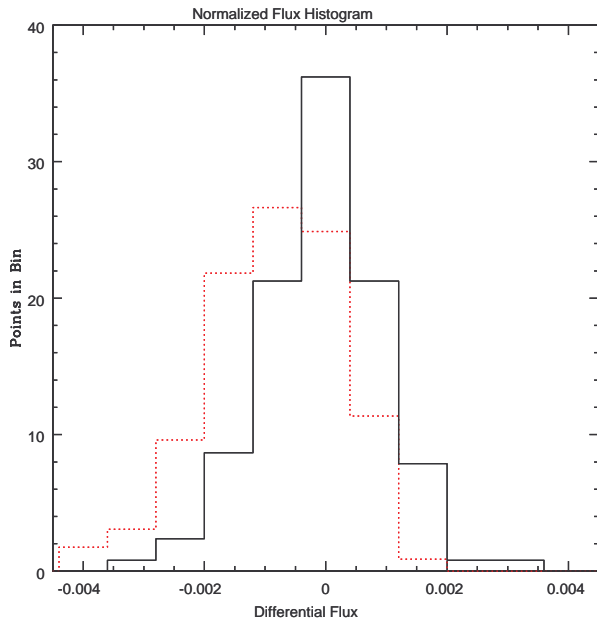


Fig. 2.— Normalized flux histograms of the in-eclipse (dotted red line) and out-of-eclipse (solid line) portions of the WASP-12 light curve in Figure 1. The bin width is 0.00082 in differential flux, coincident with the detected eclipse depth.

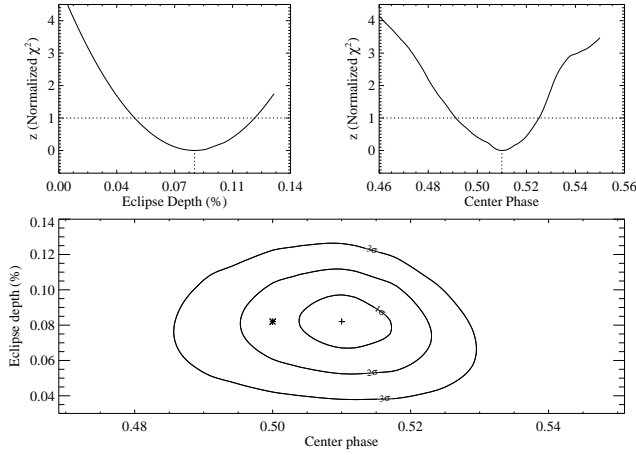


Fig. 3.— *Top*: Model eclipse 1-D cuts through the normalized- χ^2 parameter space for the eclipse depth and center phase. $z=0$ gives the best fit and $z=1$ shows the 1σ confidence interval. *Bottom*: Contour plot of the eclipse depth versus the center phase, where the 1σ depth error has been fixed to 0.015%. The best model fit is indicated by the cross symbol at $\phi=0.51$ and depth = 0.082%, together with 1σ to 3σ confidence contours. The star symbol at $\phi=0.50$ corresponds to a circular orbit.

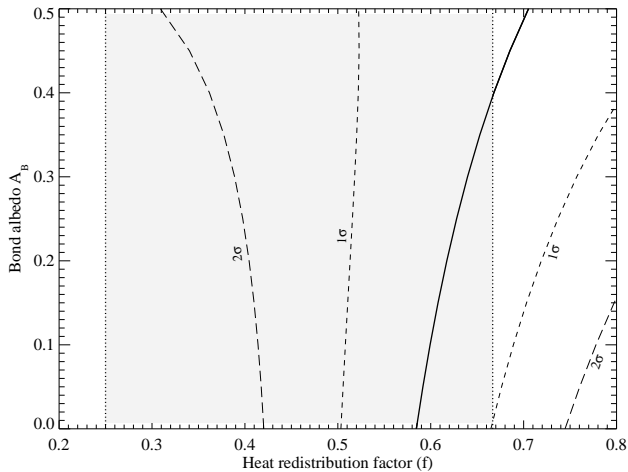


Fig. 4.— Values of A_B and f that reproduce the observed z' -band eclipse depth of WASP-12b, assuming the planet emits as a blackbody. The shaded area highlights the region of allowed f values ($1/4 - 2/3$). The short and long dashed lines delimit, respectively, the 1σ and 2σ confidence regions of the result.

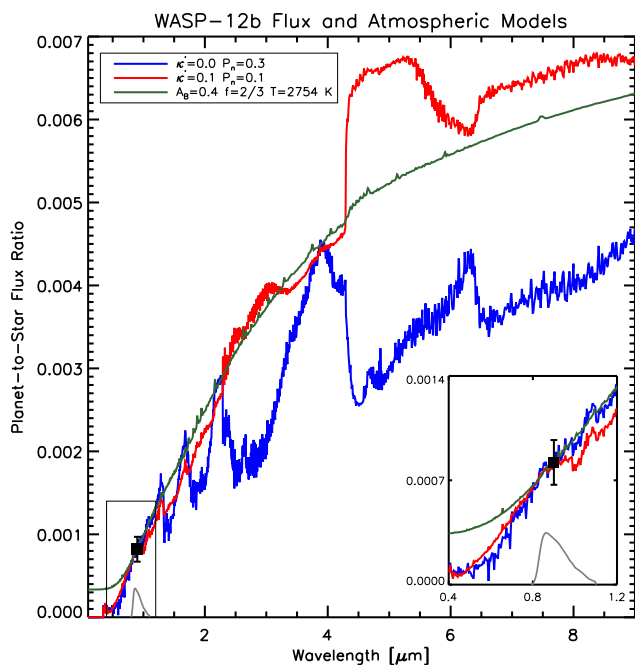


Fig. 5.— Comparison of the eclipse depth (planet-to-star flux ratio) to models. The green line shows the $A_B = 0.4$, $f = 2/3$ blackbody model from Figure 4. The blue and red lines show, respectively, the best fit model for an atmosphere with no extra absorber, and with an extra absorber of opacity κ' between 0.43 and 1.0 μm . The black thin line at the bottom indicates the SPICam plus SDSS z' -band filter response. See §3 for more details.